Journal of Materials Chemistry A

ROYAL SOCIETY OF CHEMISTRY

PAPER

Published on 21 September 2026
Licensed under CC-BY 4.0

Check for updates

Cite this: *J. Mater. Chem. A*, 2026, **14**, 42453

Direct observation and quantitative analysis of lithium diffusion in LLNbO single crystals *via* isotope tracing and TOF-SIMS

Prince Sharma, [a] Gen Hasegawa, [ae] Kaori Sugii, [a] Yasuyuki Fujiwara, [c] Hideki Iba[ad] and Naoaki Kuwata *[ab]

Understanding intrinsic ion transport in solid electrolytes is essential for the development of high-performance all-solid-state batteries. However, quantitative evaluation of bulk diffusion, decoupled from grain-boundary contributions, remains challenging, particularly in fast-ion-conducting materials. In this study, we establish a methodology for quantitatively extracting intrinsic lithium-ion diffusion coefficients in single-crystalline solid electrolytes using time-of-flight secondary ion mass spectrometry (TOF-SIMS) combined with ^{6}Li isotope exchange. Perovskite-type $La_{(1-x)/3}Li_xNbO_3$ ($x = 0.08$, LLNbO) is employed as a model system due to its high lithium-ion conductivity and structural stability. ^{6}Li isotope exchange is carried out using $^{6}LiNO_3$ solution, followed by controlled thermal annealing to induce diffusion. High-resolution TOF-SIMS is used to obtain spatially resolved lithium concentration profiles. The diffusion profiles were initially analysed using analytical solutions of Fick's second law. The final bulk diffusion coefficients were then determined using a two-dimensional numerical diffusion model that accounts for finite-size effects and the finite sample geometry. This analytical framework enables reliable reconstruction of diffusion profiles and quantitative extraction of intrinsic bulk diffusion coefficients over a wide range of temperatures and timescales. The proposed methodology provides a general approach for quantitative microscale characterization of ion transport in solid-state materials and offers a useful framework for the design of advanced solid electrolytes.

Received 9th April 2026
Accepted 3rd September 2026

DOI: 10.1039/d6ta03003c

rsc.li/materials-a

Introduction

There is a great need for the development of next-generation electrochemical energy storage systems, specifically all-solid-state batteries, for which the central need is to understand ion transport in solid electrolytes (SEs).[1–4] Generally, all the key battery performance metrics including rate capability, ionic conductivity, long-term stability and interfacial charge transfer are fundamentally governed by the ionic transport in SEs.[5,6] However, elucidating intrinsic ion transport mechanisms remains challenging due to the complex interplay of microstructural features such as grain boundaries, phase heterogeneity, and defect distributions.[7–11] In most polycrystalline SEs, these extrinsic factors often dominate ionic conduction, obscuring the true bulk transport properties governed by lattice dynamics, intrinsic defect chemistry, and crystallographic anisotropy. Therefore, direct measurement of intrinsic bulk ion diffusion, free from grain boundary and interfacial contributions, is essential for establishing reliable structure–property relationships. Despite extensive efforts, experimental techniques capable of resolving intrinsic ion diffusion with both high spatial resolution and quantitative accuracy remain limited. Conventional methods such as electrochemical impedance spectroscopy (EIS) provide macroscopic conductivity but cannot unambiguously distinguish between bulk and interfacial contributions.[12–14] Pulsed-field gradient nuclear magnetic resonance (PFG-NMR) enables measurement of self-diffusion coefficients but lacks spatial resolution and may require isotopic labelling depending on the system.[10,15,16] Similarly, quasi-elastic neutron scattering (QENS) provides insights into short-range ion dynamics[17] but is constrained by large sample requirements and limited access to neutron facilities. To overcome these limitations, isotope tracer techniques combined with spatially resolved analysis offer a promising pathway for directly probing ion diffusion. In particular, time of flight secondary ion mass spectrometry (TOF-SIMS), coupled with lithium isotope exchange, enables high-resolution mapping of lithium distribution in solids.[12,18–24] However, in fast-ion-conducting solid electrolytes, accurate reconstruction of diffusion profiles is challenging due to artifacts induced by the analysis ion beam and sputtering processes, as well as the lack of standardized isotope-exchange protocols. As a result,

[a]*Center for Green Research on Energy and Environmental Materials, National Institute for Materials Science (NIMS), Tsukuba, Ibaraki 305 0044, Japan. E-mail: KUWATA.Naoaki@nims.go.jp*

[b]*Graduate School of Chemical Sciences and Engineering, Hokkaido University, Sapporo, Hokkaido 060-8628, Japan*

[c]*Faculty of Engineering, Shinshu University, Wakasato, Nagano, 380-8533, Japan*

[d]*Toyata Motor Corporation, Susono 410-1193, Japan*

[e]*Institute for Molecular Science, National Institutes of Natural Science (NINS), Okazaki, Aichi 444-8585, Japan*

the application of this approach to quantitatively extract intrinsic bulk diffusion coefficients remains limited.[10,21–23,25,26]

In this study, we establish a robust methodology for quantifying intrinsic lithium-ion diffusion in single-crystalline solid electrolytes using TOF-SIMS combined with ^{6}Li isotope exchange. By employing well-defined single-crystal systems, this approach eliminates grain boundary effects and enables direct visualization and quantification of bulk diffusion behaviour with high spatial resolution. As for a model system, we focus on perovskite-type lanthanum–lithium niobate (LLNbO) and its substituted variants, such as $La_{(1-x)/3}Li_xNbO_3$, where x represents the lithium ion concentration, which exhibit a favourable combination of high ionic conductivity and chemical stability.[7,27–34] While previous studies have reported anisotropic ionic conductivity and the influence of grain boundaries in polycrystalline samples, the intrinsic bulk diffusion behaviour in highly crystalline LLNbO has not been directly visualized.[35–37] Here, ^{6}Li isotope exchange is introduced into single-crystalline LLNbO, followed by controlled thermal annealing to induce diffusion. High-resolution TOF-SIMS was employed to obtain lithium concentration profiles in LLNbO single crystals. The diffusion profiles were initially analysed using analytical solutions of Fick's second law and subsequently refined using a two-dimensional numerical diffusion model to account for finite-size effects and the finite sample geometry, enabling quantitative determination of intrinsic bulk lithium diffusion coefficients. This methodology provides a robust framework for quantitative analysis of intrinsic lithium-ion diffusion in single-crystalline solid electrolytes. The approach presented here offers a general framework for quantitatively probing intrinsic ion diffusion in solid-state materials and provides a powerful tool for advancing the design of high-performance solid electrolytes for next-generation batteries.

Experimental section

Growth of single crystals

Single-crystalline perovskite-type $La_{(1-x)/3}Li_xNbO_3$ ($x = 0.08$) was prepared *via* a multi-step solid-state reaction followed by a seedless directional solidification process, as reported previously.[38] First, polycrystalline LLNbO was synthesized from $LiNbO_3$ and $LaNb_3O_9$ precursors. The resulting material was then processed into dense rods and subjected to directional solidification under a controlled temperature gradient to obtain bulk single crystals. The obtained crystals were cut into 4.7 × 4.7 × 0.9 mm^3 rectangular slabs and mechanically polished prior to diffusion measurements.

Isotope exchange

Lithium isotope exchange was performed using a ^{6}Li-enriched $LiNO_3$ aqueous solution (1 mol L^{-1}) following a previously reported methodology.[10] The solution was prepared by reacting $^6Li_2CO_3$ (95% ^{6}Li, Cambridge Isotope Laboratories) with concentrated HNO_3 (65 wt%, FUJIFILM Wako) in deionized water. Single-crystalline LLNbO samples (4.7 × 4.7 × 0.9 mm^3) were partially immersed in the $^6LiNO_3$ solution for different durations (47, 115, and 137 h for Samples A–C, respectively) to control the diffusion length. The thickness direction (0.9 mm) corresponds to the [001] axis, while the in-plane directions (4.7 mm) correspond to the [100]/[010] axes. Isotope exchange and subsequent diffusion measurements were carried out along the in-plane direction, *i.e.*, predominantly along the [100] axis as shown in Fig. 1. After isotope exchange, the single crystals were rapidly cooled to 163 K inside the TOF-SIMS chamber to suppress further lithium diffusion and preserve the isotope distribution. Sample A was used to evaluate room-temperature diffusion and subsequent time-dependent redistribution after storage. Samples B and C were further subjected to stepwise annealing between 300 and 523 K to investigate temperature-dependent diffusion behaviour. After each annealing step, the samples were cooled to 163 K prior to TOF-SIMS analysis. Depth profiles of ^{6}Li were obtained by TOF-SIMS, enabling quantitative analysis of lithium diffusion as a function of time and temperature. The integrated areas of the experimentally obtained isotope profiles after isotope exchange and after each annealing step were quantitatively compared, as summarized in Table S1. The integrated value used as the fitting parameter was kept constant for each sample. The experimentally obtained integrated values were in good agreement with the

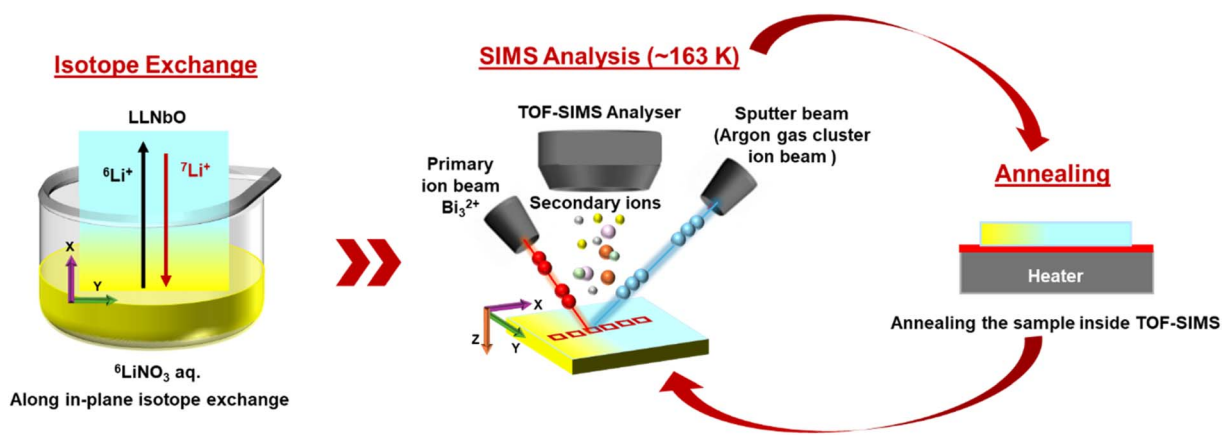


Fig. 1 Schematic representation of the ^{6}Li isotope exchange and diffusion measurement process in LLNbO.

 This journal is © The Royal Society of Chemistry 2026

corresponding fitting parameters. This quantitative agreement supports the assumption that the total amount of ^{6}Li in the sample is conserved during annealing and validates the use of the closed-system diffusion model.

X-ray diffraction (XRD)

X-ray diffraction (XRD) measurements were performed using a Rigaku SmartLab diffractometer to confirm the single-crystalline nature of LLNbO.

Impedance spectroscopy

Ionic conductivity was measured by impedance spectroscopy over the frequency range of 20 Hz to 100 MHz. Measurements between 200 and 470 K were conducted using an E4990A impedance analyser (Keysight, USA) equipped with a 4990EDMS-120K system (TOYO Corporation, Japan), while higher-temperature measurements (570–1080 K) were performed using a high-temperature system (HT-Z2-HF, TOYO Corporation, Japan). All impedance measurements were carried out on LLNbO samples with dimensions of 4.7 × 4.7 × 0.9 mm^3, where thin gold electrodes were sputtered onto opposite sides, with the electric field applied along the in-plane [100] direction.

TOF-SIMS

Prior to depth profiling, TOF-SIMS imaging was performed using a TOF-SIMS 5 instrument (IONTOF GmbH, Germany) operated at 163 K under liquid nitrogen cooling to preserve the isotope distribution during analysis. A Bi_3^{2+} primary ion beam (30 kV) was rastered over an area of 500 × 151 μm^2, providing a lateral resolution of approximately 1 × 1 μm^2. Before imaging, the sample surface was cleaned using an Ar gas cluster ion beam.

Subsequently, depth profiling was carried out using the same instrument operated at 163 K under liquid nitrogen cooling to suppress lithium diffusion during analysis. A Bi_3^{2+} primary ion beam (30 kV) was used for analysis, combined with an electron flood gun for charge compensation and Ar gas cluster ion beam (10 kV, 150 × 150 μm^2 raster) for sputtering. The use of charge neutralization was essential due to the insulating nature of LLNbO.

Diffusion analysis

The lithium concentration profiles obtained by TOF-SIMS were initially analysed using analytical solutions of Fick's second law. For diffusion lengths comparable to the sample dimensions, diffusion coefficients were subsequently refined using a two-dimensional numerical diffusion model that accounts for the finite sample geometry. The numerical model reproduces the experimentally observed concentration profiles by solving the diffusion equation under the actual sample geometry. Details of the numerical procedure are provided in the SI (Fig. S1 and S2).

Results and discussion

Crystal structure and orientation

XRD was used to characterise the crystal structure of the grown single crystal of LLNbO. The diffraction pattern shows sharp and well-defined 00l reflections, which confirms its single-crystalline nature, as shown in Fig. 2. The presence of only 00l peaks (001–006) indicates a strong preferential orientation along the c-axis. The inset illustrates the XRD measurement geometry and the crystal structure of LLNbO. These results validate the phase purity and preferred orientation of the LLNbO single crystal.

Previous studies have demonstrated that the lattice parameters of LLNbO vary systematically with Li composition.[39] The lattice parameter obtained in the present study (c = 7.891 Å) is consistent with previously reported LLNbO single crystals with Li compositions near $x \approx 0.08$, supporting the nominal composition used in this study.[40,41] Although the exact Li concentration cannot be determined solely from XRD, previous ICP-correlated studies have suggested that the high-quality crystal regions used for the present measurements correspond approximately to $x \approx 0.08$ (typically $x \approx 0.075$–0.085). Any remaining uncertainty in the Li concentration is not expected to affect the main conclusions of this work.

Ionic conductivity and diffusion coefficient from impedance spectroscopy

Fig. 3a presents the frequency dependence of the real part of the AC conductivity (σ') measured at various temperatures for the LLNbO single crystal (Sample B). In contrast to polycrystalline ceramics such as LLTO, no grain boundary contribution is observed, reflecting the single-crystalline nature of the sample. Accordingly, the observed response arises solely from bulk ionic conduction and the electrode interface. The high-frequency

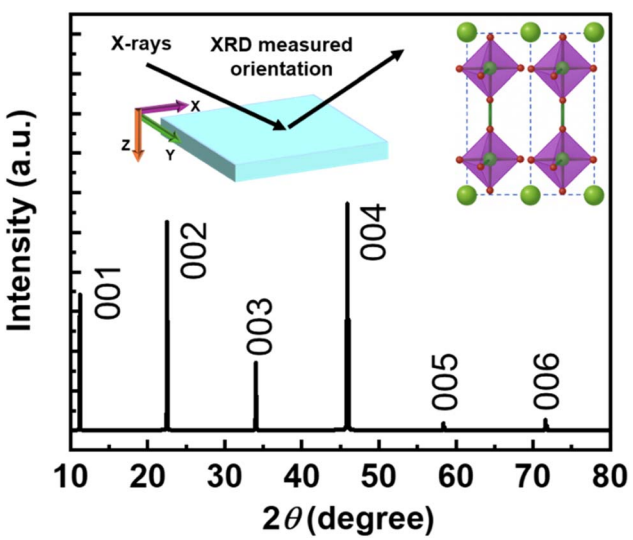


Fig. 2 XRD pattern showing only 00l reflections, confirming the single-crystalline nature and strong c-axis orientation of LLNbO. Inset: crystal structure.

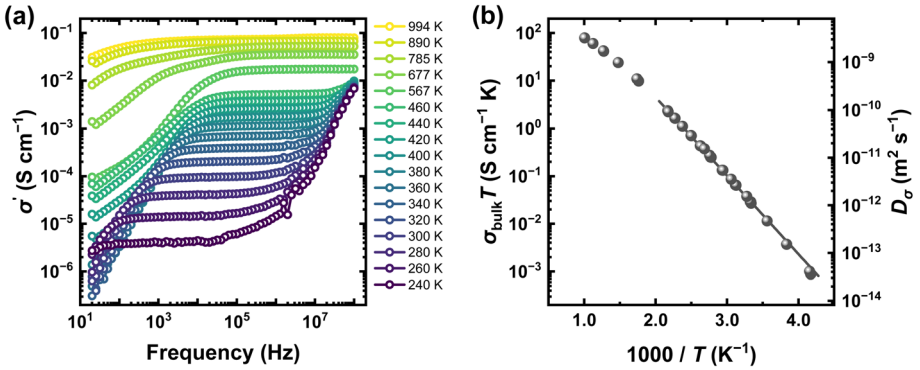


Fig. 3 (a) Frequency dependence of the real part of the AC conductivity measured at various temperatures and (b) the corresponding conductivity diffusion coefficient of LLNbO measured for Sample B.

region (10^5 to 10^8 Hz) corresponds to the intrinsic bulk response, while the low-frequency regime ($f < 10^2$ Hz) is associated with electrode polarization. The bulk ionic conductivity (σ_{bulk}) is obtained from the frequency-independent plateau in $\sigma'(f)$. Fig. 3b shows the Arrhenius plot of σ_{bulk}. Linear behaviour is observed in the temperature range 240–500 K, from which the activation energy was determined. The ionic conductivity follows the Arrhenius relation

$$\sigma_{bulk} T = \sigma_0 e^{-\frac{E_a}{k_B T}} \quad (1)$$

where σ_0 is the pre-exponential factor, E_a is the activation energy, k_B is the Boltzmann constant, and T is the absolute temperature. The activation energy derived from the linear region of the Arrhenius plot (240–500 K) is 0.33 eV, which is comparable to values reported for Li-ion transport in other perovskite-type single crystals.[7,38] Above 500 K, a slight deviation from Arrhenius behaviour is observed. Previous studies have suggested thermally induced structural modifications in LLNbO around this temperature range,[7] which may contribute to this behaviour. However, the present results do not allow us to determine the underlying mechanism.

The conductivity diffusion coefficient (D_σ) is calculated using the Nernst–Einstein relation:

$$D_\sigma = \frac{k_B T}{n z^2 e^2} \sigma_{bulk} \quad (2)$$

where z is the valence of Li^+ ($z = 1$), e is the elementary charge, k_B is the Boltzmann constant and n is the number density of Li^+ ions (1.32×10^{21} cm^{-3}). The Li-ion concentration (n) in the Nernst–Einstein equation was calculated from the nominal Li composition ($x \approx 0.08$) and the unit-cell volume determined by XRD. Although the concentration of mobile Li ions may be smaller than the total Li concentration, it has not yet been experimentally determined for LLNbO. Therefore, the total Li concentration was used to calculate the conductivity-derived diffusion coefficient (D_σ). The calculated D_σ values are shown in Fig. 3b.

Visualization of the isotope distributions

Fig. 4 shows TOF-SIMS images of the relative ^{6}Li/(^{6}Li + ^{7}Li) intensity ratio near the interface (liquid level) in a single-crystalline LLNbO sample. Fig. 4a shows the isotope distribution after ^{6}Li exchange at 300 K for 138 h, whereas Fig. 4b shows the distribution after subsequent annealing at 523 K for 2 h. Following isotope exchange, a concentration gradient of ^{6}Li is observed, demonstrating the replacement of ^{7}Li by ^{6}Li within the LLNbO crystal. After annealing, the concentration gradient becomes broader, indicating thermally activated bulk diffusion.

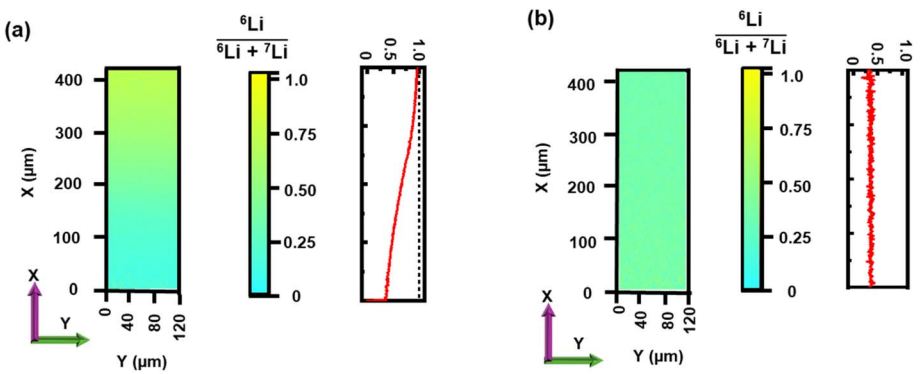


Fig. 4 TOF-SIMS images of the relative ^{6}Li/(^{6}Li + ^{7}Li) intensity ratio in the ab-plane of a single-crystalline LLNbO sample, where the vertical axis corresponds to the diffusion direction. (a) After ^{6}Li isotope exchange at 300 K for 138 h and (b) after subsequent annealing at 523 K for 2 h. The broader ^{6}Li distribution after annealing indicates thermally activated Li diffusion.

 This journal is © The Royal Society of Chemistry 2026

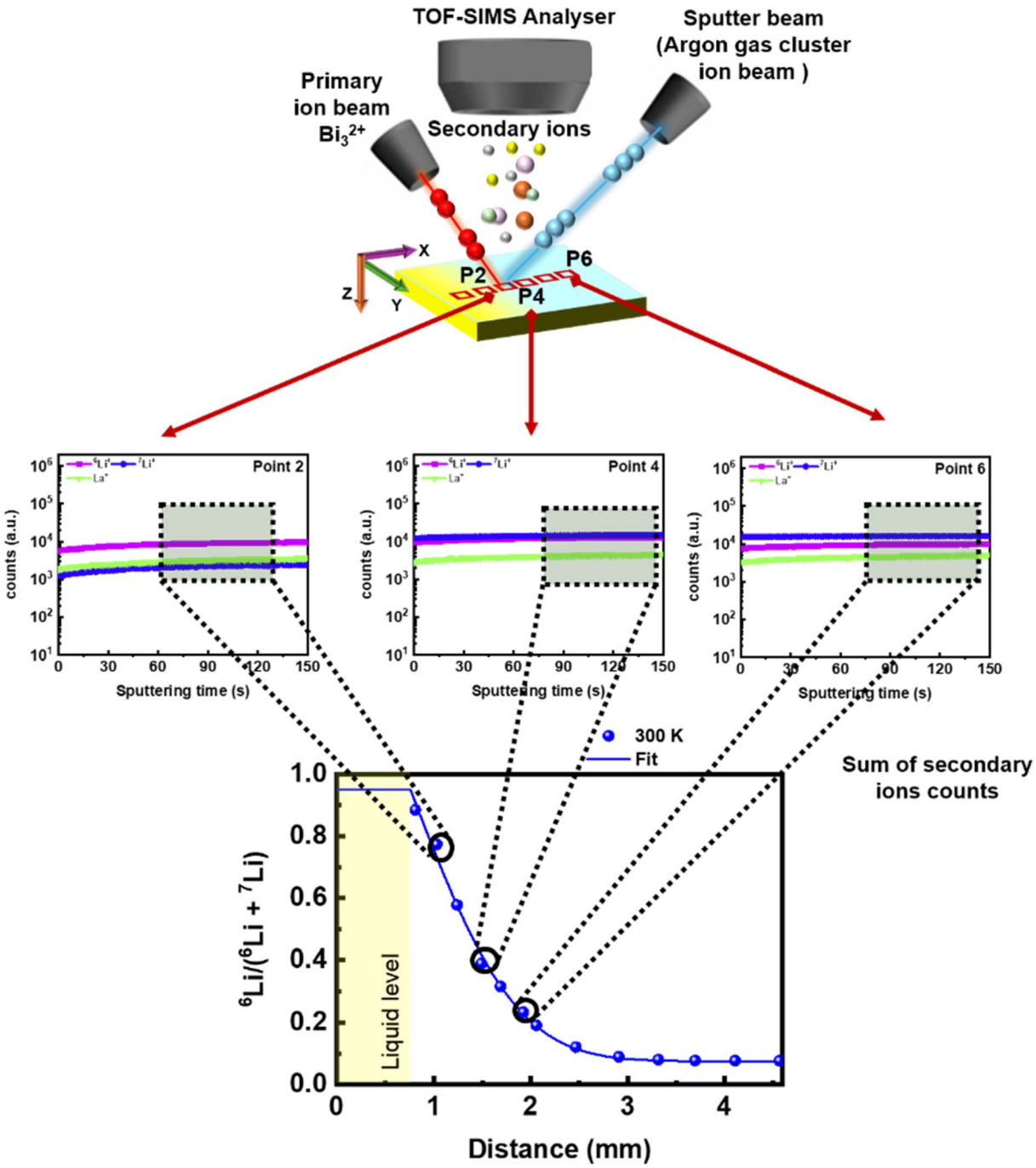


Fig. 5 Schematic illustration of the procedure used to construct one-dimensional isotope concentration profiles from TOF-SIMS depth profiling.

Notably, no features associated with grain boundary diffusion are observed, consistent with the single-crystalline nature of LLNbO. Large-area TOF-SIMS mapping performed before depth-profile analysis further confirmed the lateral uniformity of the isotope distribution over the analysed region (Fig. S3).

One-dimensional analysis of tracer diffusion profiles

To quantify lithium tracer diffusion, one-dimensional isotope concentration profiles were constructed from TOF-SIMS depth profiling, as illustrated in Fig. 5. Pointwise measurements were performed along the diffusion direction, starting from the interface with the ^{6}Li-enriched solution (liquid level) and extending into the bulk crystal. At each position (*e.g.* points 2, 4, and 6 in Fig. 5), a TOF-SIMS depth profile was acquired, and the integrated ^{6}Li and ^{7}Li signal intensities were used to determine the local isotope fraction. This procedure was repeated for all three samples. Depth profiling was conducted over a 50 × 50 μm^2 area using 150 sputtering cycles (1 s per cycle),

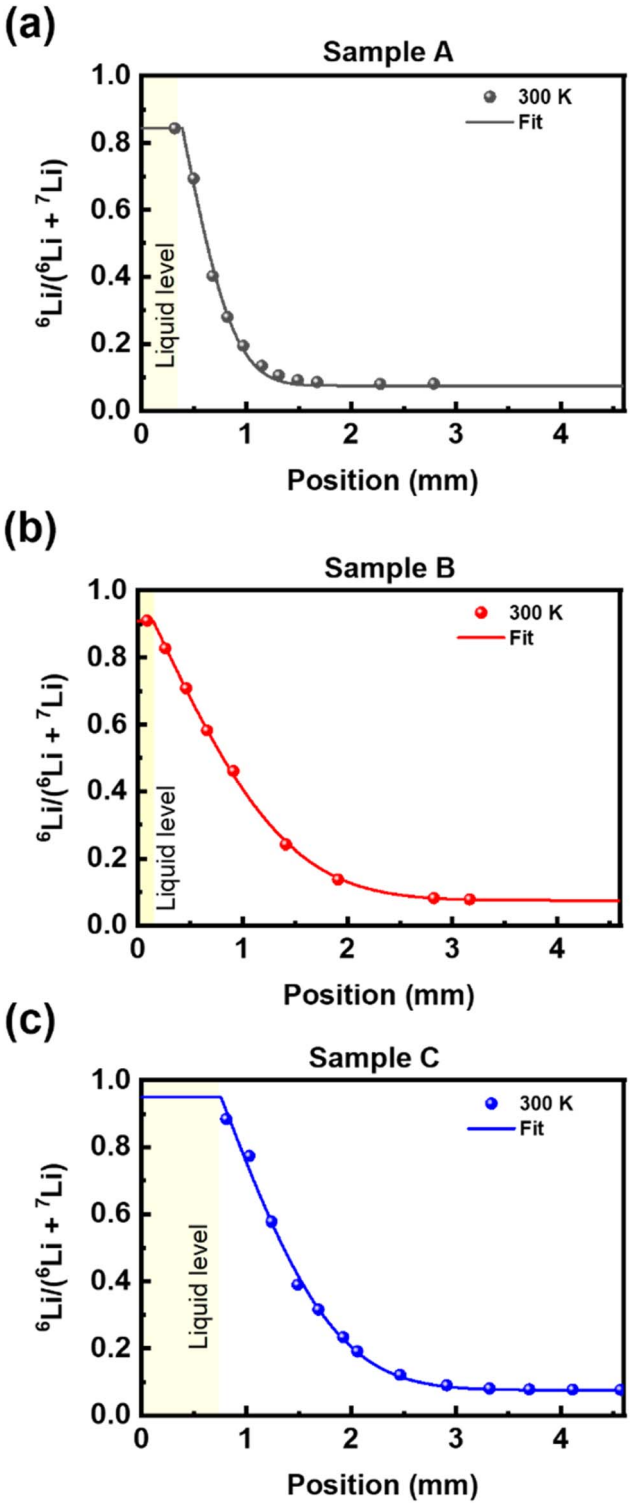


Fig. 6 One-dimensional ^{6}Li isotope concentration profiles of (a) Sample A, (b) Sample B and (c) Sample C after isotope exchange at 300 K for 47, 115, and 137 h, respectively.

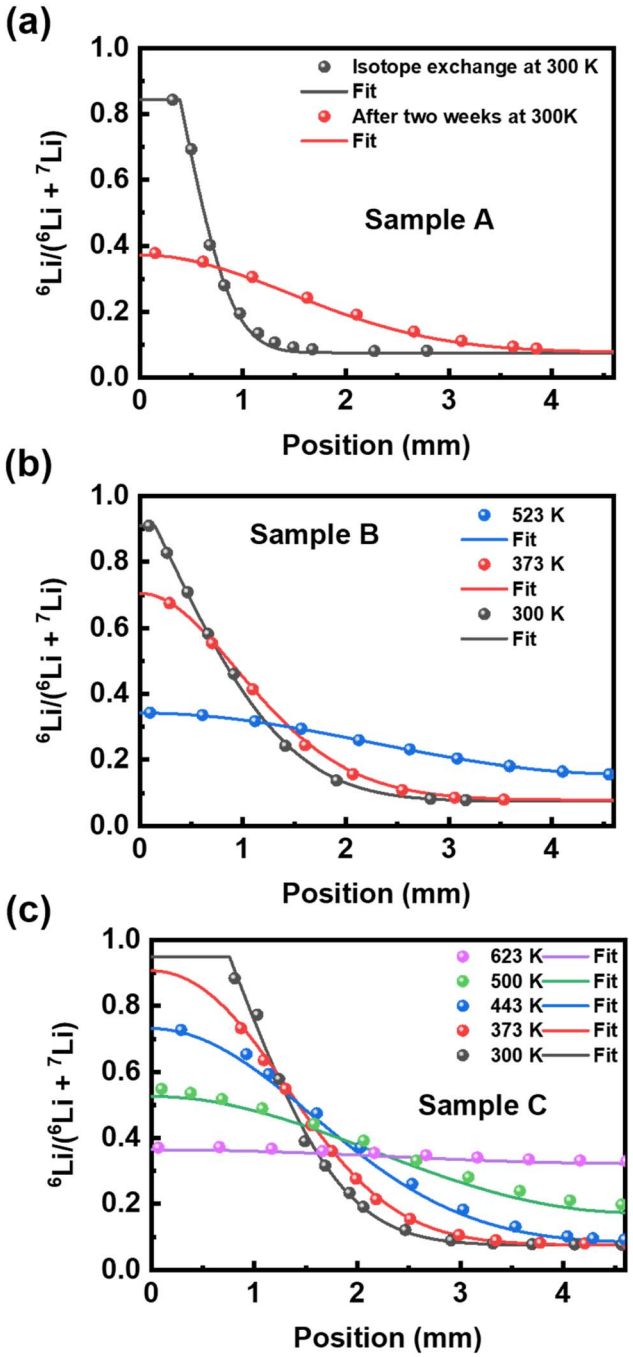


Fig. 7 (a) One-dimensional ^{6}Li isotope concentration profile of Sample A after isotope exchange at 300 K for 47 h, followed by storage under ambient conditions for two weeks. The solid line represents the fitted profile based on eqn (7). (b and c) One-dimensional ^{6}Li isotope concentration profiles of Samples B and C after annealing at different temperatures (300–623 K). The solid lines represent the fitted profiles based on eqn (7).

corresponding to a total sputtering time of 150 s. The sputtering depth was calibrated by measuring the depth of a TOF-SIMS sputtered crater using a laser microscope after sputtering under the same experimental conditions (Fig. S4). Based on the measured sputtering rate, the analysis depth after 150 s was estimated to be approximately 60 nm. Representative depth profiles for all samples and conditions are provided in Fig. S5–S14. The m/z spectrum (Fig. S15) confirms the clear detection of both ^{6}Li and ^{7}Li isotopes.

This journal is © The Royal Society of Chemistry 2026

The local ^{6}Li isotope fraction is calculated as:[42]

$$C = \frac{I_{^6\mathrm{Li}}}{I_{^6\mathrm{Li}} + I_{^7\mathrm{Li}}} \quad (3)$$

where $I_{^6\mathrm{Li}}$ and $I_{^7\mathrm{Li}}$ are the respective TOF-SIMS signal intensities. To determine the local isotope fraction, the ^{6}Li and ^{7}Li intensities were averaged over the sputtering time range of 60–120 s, corresponding to the stable region of the depth profile (Fig. 5). This range was selected to avoid surface-related artifacts and transient signal variations at the beginning of sputtering.

Fig. 6 presents the one-dimensional ^{6}Li isotope concentration profiles obtained after isotope exchange at 300 K for 47 h (Sample A), 115 h (Sample B), and 137 h (Sample C). In all samples, the ^{6}Li fraction decreases monotonically with increasing distance from the original liquid level, demonstrating inward tracer diffusion into the crystal. As expected for Fickian diffusion, the diffusion profiles broaden with increasing exchange time, indicating progressive penetration of ^{6}Li into the crystal. To obtain an initial estimate of the lithium tracer diffusion coefficient, the experimental concentration profiles were analyzed using the one-dimensional analytical solution of Fick's second law. Because the measurements were performed on single-crystalline LLNbO, grain-boundary diffusion is absent, as confirmed by the TOF-SIMS images (Fig. 4). Therefore, the analytical model describes lattice diffusion only. When a sample is brought into contact with an isotope reservoir of sufficiently large capacity, the concentration profile is described by the semi-infinite solution to Fick's second law [43,44]:

$$\frac{C(x) - C_0}{C_S - C_0} = \mathrm{erfc}\left(\frac{x}{2\sqrt{D_0 t_0}}\right) \quad (4)$$

Here, C_S is the isotope concentration in the diffusion source, C_0 is the initial isotope concentration in the sample, D_0 is the diffusion coefficient during the isotope exchange, and t_0 is the exchange time. In the present experiment, however, only part of the sample was in contact with the isotope solution,[43–45] allowing the concentration profile to be approximated by:

$$C(x) = \begin{cases} C_S & 0 \le x < h \\ (C_S - C_0)\mathrm{erfc}\left(\dfrac{x-h}{2\sqrt{D_0 t_0}}\right) + C_0 & h \le x \end{cases} \quad (5)$$

where h is the distance from the sample edge to the liquid level.

By fitting eqn (5) to the experimental concentration profiles, initial estimates of the lithium tracer diffusion coefficients were obtained for Samples A–C. Overall, the analytical solution reproduced the measured concentration profiles reasonably well, indicating that one-dimensional Fickian diffusion provides an appropriate first approximation for lithium transport in single-crystalline LLNbO. However, as discussed below, this analytical model does not fully account for the finite sample geometry, and the diffusion coefficients were therefore further refined using two-dimensional numerical analysis.

Following the room-temperature isotope exchange, Sample A was stored under ambient conditions for an additional two weeks to evaluate the temporal evolution of the diffusion profile at room temperature without further contact with the ^{6}Li-enriched solution. In contrast, Samples B and C were annealed inside the TOF-SIMS chamber in the temperature range 300–673 K for 2 h at each temperature. After each annealing step, the samples were rapidly cooled to 163 K to suppress further diffusion.

Because these post-exchange diffusion processes occurred without contact with an external isotope source, the constant surface concentration boundary condition used in eqn (5) was no longer applicable. Instead, the concentration profiles were analyzed using the analytical solution of Fick's second law for a finite closed system of length L. For an arbitrary initial isotope distribution $f(x)$, the general solution is given by[43]

$$C(x,t) = \frac{1}{L}\int_0^L f\left(x'\right)\mathrm{d}x' + \frac{2}{L}\sum_{n=1}^{\infty}\exp\left(-\frac{n^2\pi^2 D_1 t_1}{L^2}\right)\cos\left(\frac{n\pi x}{L}\right)\int_0^L f\left(x'\right)\cos\left(\frac{n\pi x'}{L}\right)\mathrm{d}x' \quad (6)$$

here, L is the sample length, D_1 is the diffusion coefficient at the annealing temperature, and t_1 is the annealing time. By substituting the initial profile obtained from eqn (5), the concentration profile is expressed as:

$$\begin{aligned}\frac{C(x,t) - C_0}{C_S - C_0} = {} & \frac{h}{L} + \frac{L-h}{L}\mathrm{erfc}\left(\frac{L-h}{2\sqrt{D_0 t_0}}\right) \\ & + \frac{2}{L}\sqrt{\frac{D_0 t_0}{\pi}}\left\{1 - \exp\left[-\frac{(L-h)^2}{4D_0 t_0}\right]\right\} \\ & + \frac{2}{\pi}\sum_{n=1}^{\infty}\frac{A_n}{n}\exp\left(-\frac{n^2\pi^2 D_1 t_1}{L^2}\right)\cos\left(\frac{n\pi x}{L}\right)\end{aligned} \quad (7)$$

The coefficient A_n is defined as:

$$A_n = \frac{2}{\sqrt{\pi}}\int_0^{\frac{L-h}{2\sqrt{D_0 t_0}}} d\xi \exp\left(-\xi^2\right)\sin\left[\frac{n\pi\left(2\sqrt{D_0 t_0}\times\xi + h\right)}{L}\right] \quad (8)$$

with L, h, D_0 and t_0 fixed, the coefficient A_n is uniquely determined for each value of n. Accordingly, D_1 was the only adjustable fitting parameter.

The parameters C_S, C_0, h, D_0 and t_0, obtained by fitting the post-exchange profile with eqn (5), were fixed during the analysis, and the sample length was set to $L = 4.7$ mm. The total amount of ^{6}Li in the sample, estimated from the post-exchange profiles, was conserved during annealing, supporting the use of the profile obtained from eqn (5) as the initial condition for the

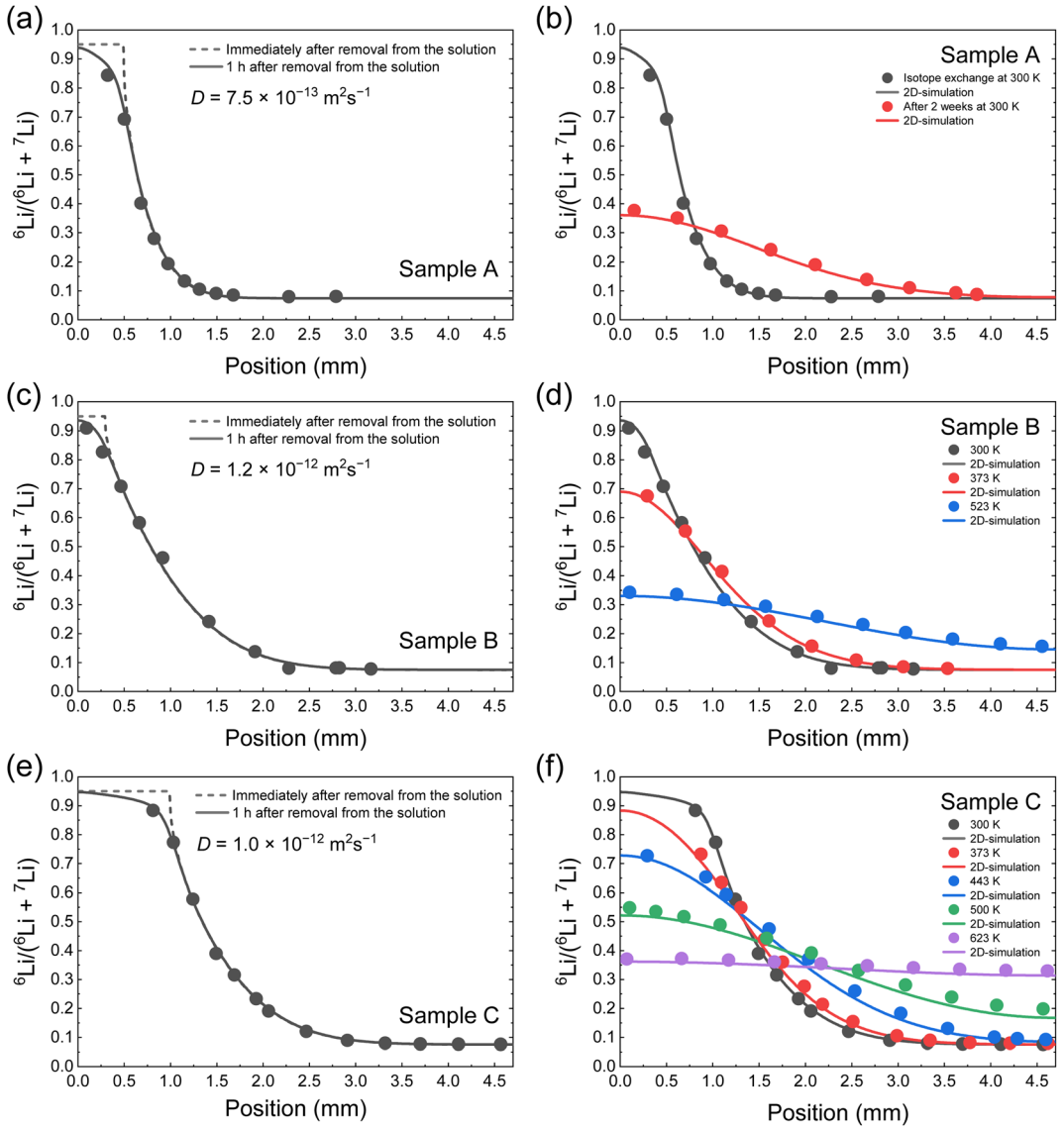


Fig. 8 Experimental ^{6}Li isotope concentration profiles and corresponding two-dimensional numerical simulations for Samples A–C. (a, c and e) Profiles immediately after isotope exchange at 300 K for Samples A, B, and C, respectively. The dashed lines indicate the isotope distributions immediately after removal from the isotope source, which were used as the initial conditions for the one-hour diffusion simulations shown by the solid lines. The one-hour diffusion time corresponds approximately to the time between removal from the isotope source and the start of the TOF-SIMS measurement. (b, d and f) Temperature-dependent isotope concentration profiles for Samples A, B, and C, respectively. Filled circles and solid lines represent the experimental data and the corresponding two-dimensional numerical simulations, respectively. The simulations assumed that the lithium diffusion coefficient along the thickness direction ([001]) was one-third of that along the in-plane direction, based on the ionic-conductivity anisotropy. The diffusion coefficients were determined by fitting the simulated concentration profiles to the experimental data.

subsequent diffusion analysis. This analytical approach accounts for the finite sample geometry during post-exchange annealing.[43,46,47]

Fig. 7a compares the isotope concentration profiles of Sample A measured immediately after isotope exchange and after subsequent storage for two weeks at room temperature under ambient conditions. The fitted profiles reproduced the experimental concentration profiles well and were used to determine the diffusion coefficients. The profile broadening observed after storage indicates that lithium redistribution continues within the crystal under the internal concentration gradient even after removal from the isotope solution.

Fig. 7b and c show the experimental and fitted ^{6}Li profiles for Samples B and C after annealing at different temperatures. The fitted profiles reproduce both the concentration gradients and diffusion length observed experimentally. Furthermore, at elevated temperatures, the isotope concentration profiles become flatter owing to enhanced lithium diffusion, resulting in increased uncertainty in the fitted diffusion coefficients. Nevertheless, the concentration profiles remain sufficiently

 This journal is © The Royal Society of Chemistry 2026

Table 1 Comparison of the lithium tracer diffusion coefficients in LLNbO obtained from the one-dimensional analytical fitting and the two-dimensional numerical simulation of the TOF-SIMS isotope concentration profiles. The average diffusion coefficient obtained from four measurements at 300 K is 9.3×10^{-13} m^2 s^{-1}, with a relative standard deviation of approximately 20%. This variation provides an estimate of the experimental uncertainty in the room-temperature diffusion measurements

Sample	Temperature (K)	Diffusion coefficient from 1D analytical fitting (m^2 s^{-1})	Diffusion coefficient from 2D numerical simulation (m^2 s^{-1})
Sample A	300	4.5×10^{-13}	7.5×10^{-13}
	300 (for two weeks)	7.4×10^{-13}	7.4×10^{-13}
Sample B	300	1.2×10^{-12}	1.2×10^{-12}
	373	1.5×10^{-11}	1.5×10^{-11}
	523	3.1×10^{-10}	3.1×10^{-10}
Sample C	300	7.4×10^{-13}	1.0×10^{-12}
	373	2.4×10^{-11}	1.4×10^{-11}
	443	6.7×10^{-11}	6.7×10^{-11}
	500	1.8×10^{-10}	1.8×10^{-10}
	623	6.2×10^{-10}	6.2×10^{-10}

well-defined for reliable diffusion analysis. These isotope concentration profiles served as the basis for the subsequent two-dimensional numerical analysis described in the following section.

Two-dimensional numerical diffusion analysis

Although the one-dimensional analytical solution provides a useful first approximation, finite-size effects associated with the actual sample geometry are not explicitly considered. To evaluate their influence on the measured isotope concentration profiles, a two-dimensional numerical analysis was performed. Details of the simulation model, numerical procedure, initial conditions, and boundary conditions are provided in the SI.

Representative comparisons between the experimental isotope concentration profiles and the corresponding two-dimensional numerical fits are shown in Fig. 8. The numerical model successfully reproduced both the shape and the diffusion length of the experimental isotope concentration profiles. The diffusion anisotropy adopted in the numerical analysis was estimated from the ionic conductivity anisotropy measured for Sample C (Fig. S16). Because Samples A and C had immersion depths comparable to the diffusion length, finite-size effects became significant and the diffusion coefficients obtained from the two-dimensional analysis were larger than those obtained from the one-dimensional analytical solution. In contrast, Sample B, which had a shallower immersion depth, showed essentially the same diffusion coefficient in both analyses.

These results indicate that the one-dimensional analytical solution tends to underestimate the diffusion coefficient when finite-size effects become significant, whereas it provides reliable estimates when such effects are negligible. The diffusion coefficients refined by the two-dimensional numerical analysis are summarized in Table 1 and were used for the Arrhenius analysis discussed below. For Sample A, the same diffusion coefficient also successfully reproduced the isotope concentration profile measured after two weeks of storage, further supporting the validity of the two-dimensional numerical analysis.

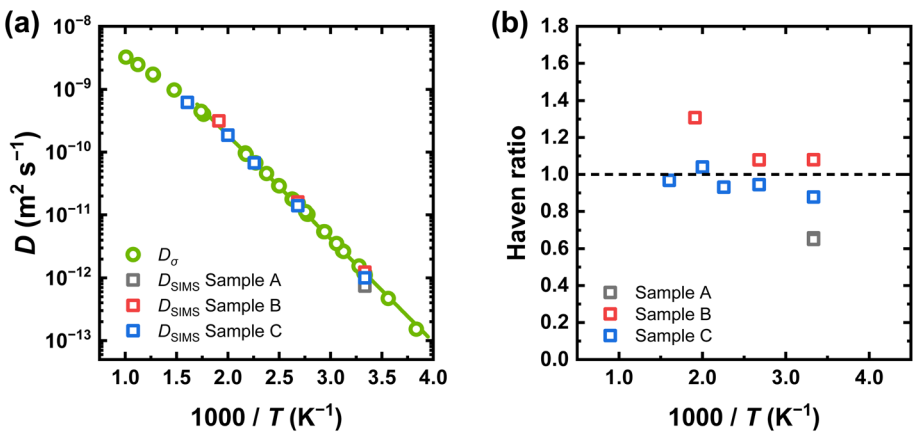


Fig. 9 (a) Arrhenius plot of the lithium tracer diffusion coefficients (D_{SIMS}) obtained by two-dimensional numerical analysis of the TOF-SIMS isotope concentration profiles, together with the conductivity diffusion coefficients (D_σ) derived from ionic conductivity measurements of LLNbO. The solid line represents the Arrhenius fit to the low-temperature diffusion coefficients, yielding an activation energy of 0.33 eV. (b) Temperature dependence of the Haven ratio calculated from the refined lithium tracer diffusion coefficients and the conductivity diffusion coefficients.

The two-dimensional numerical analysis also led to a revision of the diffusion coefficient for Sample C at 373 K after removal from the isotope source. During the relatively short diffusion period after sample removal, the isotope concentration near the region previously in contact with the isotope source can decrease not only by in-plane diffusion but also by diffusion in the thickness direction. When such a profile is analysed using a one-dimensional diffusion model, this additional concentration decrease can be interpreted as faster in-plane diffusion, leading to an overestimation of the in-plane diffusion coefficient. By explicitly accounting for diffusion in the thickness direction, the two-dimensional analysis therefore gives a lower diffusion coefficient at 373 K than the one-dimensional analysis.

The refined lithium tracer diffusion coefficients obtained from the two-dimensional numerical analysis are compared with the conductivity diffusion coefficients derived from ionic conductivity measurements in Fig. 9a. Within the investigated temperature range, the two diffusion coefficients are in good agreement and exhibit similar temperature dependencies, although only a limited number of tracer diffusion data points were obtained at elevated temperatures.

The resulting Haven ratios (D_{SIMS}/D_{σ})[48,49] are shown in Fig. 9b. No clear temperature dependence was observed over the investigated temperature range, although some scatter was present. The average Haven ratio was 0.95, indicating that the tracer and conductivity diffusion coefficients are generally comparable. Although this value is higher than the typical Haven ratio of ~0.5 reported for conventional oxide electrolytes, similar behaviour has been reported for perovskite-type solid electrolytes with low Li concentrations,[10] where Li ions are considered to migrate in a largely uncorrelated manner.

LLNbO has a double-perovskite structure, in which La and Li occupy A-sites within the same layer. For the composition $x = 0.08$, the occupancies of La, Li, and vacancies on the A-sites in this layer are approximately 0.61, 0.16, and 0.23, respectively. Considering only Li-accessible sites, the vacancy fraction is estimated to be approximately 59%, indicating that more than half of the Li-accessible sites are vacant. This low Li occupancy and high vacancy fraction are expected to reduce correlation effects during Li-ion migration, which is consistent with the observed Haven ratio close to unity.

Within the investigated temperature range, the tracer diffusion coefficients exhibit a temperature dependence consistent with that of the low-temperature conductivity diffusion coefficients, which yield an activation energy of 0.33 eV. The good agreement between the tracer and conductivity diffusion coefficients further supports the validity of the present diffusion analysis.

Conclusion

Lithium tracer diffusion in single-crystalline LLNbO was systematically investigated by combining ^{6}Li isotope exchange with TOF-SIMS depth profiling performed at multiple positions along the diffusion direction. To improve the accuracy of the diffusion analysis, the isotope concentration profiles were analyzed using both one-dimensional analytical fitting and two-dimensional numerical simulation that accounts for finite-size effects. The refined tracer diffusion coefficients obtained from the two-dimensional numerical analysis showed good agreement with the conductivity diffusion coefficients derived from ionic conductivity measurements. The corresponding Haven ratio was close to unity, indicating largely uncorrelated lithium-ion migration in LLNbO. The high vacancy fraction on the Li-accessible A-sites is considered to reduce correlation effects during lithium-ion migration, providing a structural origin for the observed Haven ratio. The present methodology, combining lithium isotope exchange, TOF-SIMS profiling, and two-dimensional numerical analysis, provides a reliable and quantitative approach for determining lithium tracer diffusion coefficients, particularly in fast lithium-ion conductors where finite-size effects become significant.

Author contributions

Prince Sharma performed the isotope exchange experiments, conducted TOF-SIMS measurements and analysis, and prepared the initial draft of the manuscript. Gen Hasegawa contributed to TOF-SIMS measurements, data analysis, and critical revision of the manuscript. Kaori Sugii performed the temperature-dependent ionic conductivity measurements. Yasuyuki Fujiwara prepared the single-crystal samples, contributed to compositional analysis, and participated in data interpretation and discussion. Hideki Iba contributed to project planning, data interpretation, and scientific discussions. Naoaki Kuwata conceived and supervised the project, contributed to data interpretation, and revised and finalized the manuscript.

Conflicts of interest

The authors declare no competing financial interest.

Data availability

The data supporting the findings of this study are available within the article and its supplementary information (SI). Additional raw data, including TOF-SIMS depth profiles and isotope diffusion datasets, are available from the corresponding author upon reasonable request. Supplementary information is available. See DOI: https://doi.org/10.1039/d6ta03003c.

Acknowledgements

This study is supported by the JST COI-NEXT “Center for Advanced Battery Collaboration” (grant number JPMJPF2016), JSPS KAKENHI (grant number 24KF0271), and JST GteX Program (grant number JPMJGX23S2). This work is partly supported by JSPS KAKENHI (grant number 24H02205 (Ion Jamology)), NIMS All-Solid-State Battery Materials Open Platform (MOP), and SOLiD-Next (JPNP23005), subsidized by the New Energy and Industrial Technology Development

 This journal is © The Royal Society of Chemistry 2026

Organization (NEDO). The TOF-SIMS and XRD measurements are supported by the NIMS Battery Research Platform.

References

1 C. Li, Z. Yu Wang, Z. Jiang He, Y. Jiao Li, J. Mao, K. Hua Dai, C. Yan and J. Chao Zheng, *Sustain. Mater. Technol.*, 2021, **29**, e00297.
2 J. Janek and W. G. Zeier, *Nat. Energy*, 2023, **8**, 230–240.
3 W. D. Richards, L. J. Miara, Y. Wang, J. C. Kim and G. Ceder, *Chem. Mater.*, 2016, **28**, 266–273.
4 Y. Xiao, Y. Wang, S. H. Bo, J. C. Kim, L. J. Miara and G. Ceder, *Nat. Rev. Mater.*, 2020, **5**, 105–126.
5 J. Maier, *Nat. Mater.*, 2005, **4**, 805–815.
6 *Springer Series in Solid-State Sciences*, ed. H. Mehrer, Springer Berlin Heidelberg, Berlin, Heidelberg, 2007, vol. 155, pp. 1–23.
7 X. Hu, C. A. J. Fisher, S. Kobayashi, Y. H. Ikuhara, Y. Fujiwara, K. Hoshikawa, H. Moriwake, K. Kohama, H. Iba and Y. Ikuhara, *Acta Mater.*, 2018, **156**, 379–388.
8 H. Lian, X. Hu, D. Xiong, S. Tao, B. Zhong, B. Song, W. Deng, H. Hou, G. Zou and X. Ji, *Energy Storage Mater.*, 2024, **71**, 103593.
9 D. Wang, H. Shi, S. Wang, X. Wu, W. Jiang, S. Liang and Z. Xu, *Coord. Chem. Rev.*, 2024, **508**, 215776.
10 G. Hasegawa, N. Kuwata, K. Hashi, Y. Tanaka and K. Takada, *Chem. Mater.*, 2023, **35**, 3815–3824.
11 G. Hasegawa, N. Kuwata, T. Ohnishi and K. Takada, *J. Mater. Chem. A*, 2023, **12**, 731–738.
12 I. O. Santos-Mendoza, J. Vázquez-Arenas, I. González, G. Ramos-Sánchez and C. O. Castillo-Araiza, *Int. J. Chem. React. Eng.*, 2019, **17**, 20180095.
13 B. Tian, J. Światowska, V. Maurice, S. Zanna, A. Seyeux, L. H. Klein and P. Marcus, *J. Phys. Chem. C*, 2013, **117**, 21651–21661.
14 V. F. Lvovich, *Impedance Spectroscopy: Applications to Electrochemical and Dielectric Phenomena*, John Wiley & Sons, Inc., Hoboken, NJ, USA, 2012.
15 X. Liu, Z. Liang, Y. Xiang, M. Lin, Q. Li, Z. Liu, G. Zhong, R. Fu and Y. Yang, *Adv. Mater.*, 2021, **33**, 2005878.
16 F. Blanc, M. Leskes and C. P. Grey, *Acc. Chem. Res.*, 2013, **46**, 1952–1963.
17 M. Matsuura, Y. Fujiwara, H. Moriwake, K. Ohara and Y. Kawakita, *Phys. Rev. B*, 2021, **104**, 94305.
18 J. F. M. Oudenhoven, L. Baggetto and P. H. L. Notten, *Adv. Energy Mater.*, 2011, **1**, 10–33.
19 R. Baddour-Hadjean and J. P. Pereira-Ramos, *AIP Conf. Proc.*, 2010, **1267**, 1137–1138.
20 J. Zhu, L. Lu and K. Zeng, *ACS Nano*, 2013, **7**, 1666–1675.
21 P. Sharma, G. Hasegawa, S. Xing and N. Kuwata, *Sci. Technol. Adv. Mater.*, 2025, **26**, 2580917.
22 D. Uxa, E. Hüger, K. Meyer, L. Dörrer and H. Schmidt, *Chem. Mater.*, 2023, **35**, 3307–3315.
23 J. N. Coles and J. V. P. Long, *Philos. Mag.*, 1974, **29**, 457–471.
24 K. Watanabe, I. Sakaguchi, S. Hishita, N. Ohashi and H. Haneda, *Appl. Phys. Express*, 2011, **4**, 55801.
25 N. Molina, A. Dolocan, J. F. Curry, G. J. Rodin and F. Mangolini, *Anal. Chem.*, 2026, **98**, 5134–5140.
26 S. Xing, G. Hasegawa, P. Sharma, D. Ito, K. Kamiguchi, K. Takada and N. Kuwata, *ACS Energy Lett.*, 2026, **11**, 1889–1896.
27 W. Araki, Y. Nagakura and Y. Arai, *Ceram. Int.*, 2020, **46**, 6270–6275.
28 M. S. Ali, N. Sato, I. Fukasawa, Y. Maruyama, M. Nagao, S. Watauchi and I. Tanaka, *Cryst. Growth Des.*, 2019, **19**, 6291–6295.
29 Z. Yang, R. E. Ward, N. Tanibata, H. Takeda, M. Nakayama and T. Asaka, *J. Phys. Chem. C*, 2020, **124**, 9746–9754.
30 T. T. Choudhury, W. Araki, N. Yamada and Y. Arai, *Mater. Lett.*, 2021, **302**, 130356.
31 X. Hu, C. A. J. Fisher, S. Kobayashi, Y. H. Ikuhara, Y. Fujiwara, K. Hoshikawa, H. Moriwake, K. Kohama, H. Iba and Y. Ikuhara, *Acta Mater.*, 2017, **127**, 211–219.
32 S. García-Martín, J. M. Rojo, H. Tsukamoto, E. Morán and M. A. Alario-Franco, *Solid State Ionics*, 1999, **116**, 11–18.
33 J. Ibarra, A. Várez, C. León, J. Santamaría, L. M. Torres-Martínez and J. Sanz, *Solid State Ionics*, 2000, **134**, 219–228.
34 E. García-González, R. Marín-Gamero, M. Kuhn-Gómez, A. Kuhn, F. García-Alvarado and S. García-Martín, *J. Mater. Chem. A*, 2024, **12**, 28247–28253.
35 Y. Fujiwara, T. Taishi, K. Hoshikawa, K. Kohama and H. Iba, *Jpn. J. Appl. Phys.*, 2016, **55**, 90306.
36 M. S. Ali, Y. Maruyama, M. Nagao, S. Watauchi and I. Tanaka, *Solid State Ionics*, 2020, **350**, 115330.
37 S. Takai, T. Mandai, Y. Kawabata and T. Esaka, *Solid State Ionics*, 2005, **176**, 2227–2233.
38 Y. Fujiwara, T. Taishi and H. Iba, in *Interface Ionics: For All-Solid-State Batteries and Solid State Ionics Devices*, Springer, 2024, pp. 151–160.
39 X. Hu, S. Kobayashi, Y. H. Ikuhara, C. A. J. Fisher, Y. Fujiwara, K. Hoshikawa, H. Moriwake, K. Kohama, H. Iba and Y. Ikuhara, *Acta Mater.*, 2017, **123**, 167–176.
40 Y. Fujiwara, K. Hoshikawa and K. Kohama, Growth of solid electrolyte $La_{(1-x)}/3Li_xNbO_3$ single crystals by the directional solidification method, *J. Cryst. Growth*, 2016, **433**, 48–53.
41 X. Gao, C. A. J. Fisher, Y. H. Ikuhara, Y. Fujiwara, S. Kobayashi, H. Moriwake, A. Kuwabara, K. Hoshikawa, K. Kohama, H. Iba and Y. Ikuhara, *J. Mater. Chem. A*, 2015, **3**, 3351–3359.
42 Y. Sun, G. M. Hughes, J. Bu, J. Liu, C. R. M. Grovenor and P. S. Grant, *Micron*, 2025, **190**, 103746.
43 J. Crank, *The Mathematics of Diffusion*, Oxford University Press, 2nd edn, 1979.
44 H. Mehrer, *Diffusion in Solids: Fundamentals, Methods, Materials, Diffusion-Controlled Processes*, Springer Science & Business Media, 2007, vol. 155.
45 N. Kuwata, G. Hasegawa, D. Maeda, N. Ishigaki, T. Miyazaki and J. Kawamura, *J. Phys. Chem. C*, 2020, **124**, 22981–22992.
46 U. M. Gosele, *Annu. Rev. Mater. Sci.*, 1988, **18**, 257–282.
47 R. B. Fair, *J. Electrochem. Soc.*, 1981, **128**, 1360–1368.
48 A. Van Der Ven, Z. Deng, S. Banerjee and S. P. Ong, *Chem. Rev.*, 2020, **120**, 6977–7019.
49 G. E. Murch, *Solid State Ionics*, 1982, **7**, 177–198.